CrossMark

Forebrain knock-out of torsinA reduces striatal free-water and impairs whole-brain functional connectivity in a symptomatic mouse model of DYT1 dystonia

Jesse C. DeSimone [a], Samuel S. Pappas [b], Marcelo Febo [c], Roxana G. Burciu [a], Priyank Shukla [a], Luis M. Colon-Perez [c], William T. Dauer [b,d,e], David E. Vaillancourt [a,f,g,*]

[a] Department of Applied Physiology and Kinesiology, University of Florida, Gainesville, FL 32611, USA
[b] Department of Neurology, University of Michigan, Ann Arbor, MI 48109, USA
[c] Department of Psychiatry, College of Medicine, University of Florida, Gainesville, FL 32611, USA
[d] Department of Cell and Developmental Biology, University of Michigan, Ann Arbor, MI 48109, USA
[e] Veteran Affairs Ann Arbor Healthcare System, University of Michigan, Ann Arbor, MI 48105, USA
[f] Department of Neurology, College of Medicine, University of Florida, Gainesville, FL 32610, USA
[g] Department of Biomedical Engineering, University of Florida, Gainesville, FL 32611, USA

ARTICLE INFO

ABSTRACT

Multiple lines of evidence implicate striatal dysfunction in the pathogenesis of dystonia, including in DYT1, a common inherited form of the disease. The impact of striatal dysfunction on connected motor circuits and their interaction with other brain regions is poorly understood. Conditional knock-out (cKO) of the DYT1 protein torsinA from forebrain cholinergic and GABAergic neurons creates a symptomatic model that recapitulates many characteristics of DYT1 dystonia, including the developmental onset of overt twisting movements that are responsive to antimuscarinic drugs. We performed diffusion MRI and resting-state functional MRI on cKO mice of either sex to define abnormalities of diffusivity and functional connectivity in cortical, subcortical, and cerebellar networks. The striatum was the only region to exhibit an abnormality of diffusivity, indicating a selective microstructural deficit in cKO mice. The striatum of cKO mice exhibited widespread increases in functional connectivity with somatosensory cortex, thalamus, vermis, cerebellar cortex and nuclei, and brainstem. The current study provides the first in vivo support that direct pathological insult to forebrain torsinA in a symptomatic mouse model of DYT1 dystonia can engage genetically normal hindbrain regions into an aberrant connectivity network. These findings have important implications for the assignment of a causative region in CNS disease.

© 2017 Elsevier Inc. All rights reserved.

1. Introduction

Dystonia musculorum deformans ("Oppenheim's dystonia") is an inherited neurodevelopmental movement disorder (DYT1 dystonia) characterized by sustained, involuntary twisting movements and disabling postures (Breakefield et al., 2008; Fahn, 1988; Fahn et al., 1998; Ozelius and Lubarr, 1993). DYT1 dystonia is caused by a dominant three base-pair deletion (ΔGAG) in the *TOR1A* gene that eliminates a single glutamic acid residue (ΔE) in the C-terminus of the AAA+ protein torsinA (Ozelius et al., 1997).

Convergent evidence from human and animal studies establishes the striatum as a key region in dystonia pathophysiology. Lesion studies point to an association between disturbed putaminal integrity and clinical symptoms in patients with secondary dystonia (Bhatia and Marsden, 1994; Burton et al., 1984; Fross et al., 1987; Marsden et al., 1985). Deep brain stimulation of major striatal output targets such as the globus pallidus internus and subthalamic nucleus is an effective therapy for DYT1 dystonia (Kupsch et al., 2006; Ostrem et al., 2014; Vidailhet et al., 2005). Moreover, studies in multiple mouse models of DYT1 dystonia have implicated abnormal function of striatal cholinergic interneurons (SCI) to be involved in disruption of cortico- and thalamo-striatal synaptic integration and plasticity (Dang et al., 2012; Martella et al., 2009; Maltese et al., 2014; Pisani et al., 2006; Sciamanna et al., 2012a, 2012b). It remains unclear how striatal dysfunction affects network-level changes in functional connectivity (FC) (Biswal et al., 1995; Fox et al., 2005) across

cortical, subcortical, and cerebellar networks. Understanding how striatal pathology affects network-level FC in pre-clinical models is important for dissecting pathophysiology and providing readouts for disease modifying interventions. Further, understanding network-level connectivity in a translational model of generalized dystonia is opportune because motor impairment in human subjects with focal dystonia points to disturbances in FC (Battistella et al., 2015, 2016).

To explore these questions, we acquired in vivo diffusion MRI (dMRI) and resting-state functional MRI (rsfMRI) in a mouse model characterized by Cre-recombinase expression and conditional knockout (cKO) of torsinA from forebrain (i.e., striatum, cortex, globus pallidus, basal forebrain, and reticular thalamic nucleus) cholinergic and GABAergic neurons (Pappas et al., 2015). In contrast to human DYT1 dystonia, which does not exhibit overt structural lesions, this mouse model exhibits selective neurodegeneration specific to SCIs. As well, surviving SCIs exhibit altered morphology (i.e., hypertrophy) and dysfunctional electrophysiological properties, implicating striatal connectivity abnormalities. In turn, the structural and functional integrity of forebrain GABAergic neurons is preserved despite the lack of torsinA. We tested two hypotheses. First, we used diffusion MRI and a bi-tensor model to test the hypothesis that torsinA loss-of-function in cKO mice causes abnormal microstructural changes in free-water (FW) and tissue compartment diffusivity (free-water corrected mean diffusivity: MD_T) within the striatum. This computational approach fits a bi-tensor model to dMRI data, separating the diffusion properties of water in brain tissue from that of water in the extracellular space (Metzler-Baddeley et al., 2012; Pasternak et al., 2009). Since prior work in the cKO model demonstrated that surviving SCIs are associated with significant cellular soma hypertrophy (Pappas et al., 2015), we predicted that the extracellular FW compartment of striatal regions would be reduced, whereas the MD_T would be increased. Second, we used rsfMRI to test the hypothesis that FC is impaired between the pathologically abnormal striatum and other key cortical, subcortical, and cerebellar motor regions.

2. Materials and methods

2.1. Animals and housing

Mice originating in the Dauer Laboratory at the University of Michigan were housed and imaged at the University of Florida McKnight Brain Institute. Eighteen (10 male, 8 female; age 6.9 ± 0.8 mo) Dlx5/6-Cre$^+$ Tor1a$^{flx/-}$ (cKO) and 18 (7 male, 11 female; age 6.7 ± 1.3 mo) Cre$^-$ Tor1a$^{flx/+}$ littermate wild-type controls were used in this experiment. Mice were prepared and genotyped for Tor1a and Cre using the PCR protocol described by Liang et al. (2014) and cKO and control mice were bred as previously described (Pappas et al., 2015). Prior to animal transport, motor abnormalities (i.e., forelimb and hindlimb clasping, abnormal posturing) were confirmed in all cKO mice by postnatal days 49–56 via the tail suspension assessment (Pappas et al., 2015). Mice were housed in groups of one to three in a temperature and humidity controlled environment, maintained on an alternating 12 h. light-dark cycle (i.e., lights off at 19:00 h), and were provided ad libitum food and water access. All experimental protocols and procedures were approved and monitored by both the University of Michigan Committee on the Use and Care of Animals (UCUCA) and the University of Florida Institutional Animal Care and Use Committee (IACUC). Animals were acquired and cared for in accordance with the ethical standards set forth by the Guide for the Care and Use of Laboratory Animals (8th Edition, 2011) and the American Association for Laboratory Animal Science guidelines.

2.2. MRI preparation and data acquisition

Experimenters involved in data collection had no a priori knowledge of the genotype of each animal during MRI acquisition, and the blind

was not broken until the final between-group statistics were performed. Mice were anesthetized for the duration of the experiment. Isoflurane anesthesia was delivered using compressed air through a Surgivet vaporizer (Dublin, OH, USA) connected to a charcoal trap. Mice were initially induced at 3–4% isoflurane for 1–2 min in an enclosed knock-in chamber. Anesthesia was reduced to 2% for animal setup and 1.0–1.5% for MRI acquisition. Notably, this level of anesthesia was considered appropriate based on previous evidence that concentrations within this bandwidth preserve FC patterns in rodent models (Ferron et al., 2009; Liu et al., 2013). Animals were placed in a prone position on a custom design plastic mouse bed equipped with a bite bar that served to immobilize the head and deliver anesthesia during scanning. An in-house 2.5 × 3.5 cm quadrature surface transmit/receive coil (Advanced Magnetic Resonance Imaging and Spectroscopy Facility, University of Florida, Gainesville, FL, USA) was affixed to the top of the skull and tuned to 470.7 MHz (^{1}H resonance) for B^1 excitation and signal detection. Respiratory vitals and core body temperature (37–38 °C) were monitored and maintained using a respiration pad and a recirculating waterbed heating system (SA Instruments, Stony Brook, NY, USA).

MRI data were acquired using an 11.1 Tesla Magnex Scientific horizontal magnet (Agilent, Inc., Santa Clara, CA, USA, 205/120HD gradient set with 120 mm inner gradient bore size; maximum gradient strength 600 mT/m and rise time of 130 μs) at the University of Florida McKnight Brain Institute. MRI sequences were prepared and acquired using VNMRJ software (Agilent Technologies, Version 3.1) and included acquisition of anatomical scout sequences for real-time visual depiction of brain positioning, as well as whole-brain voxel shimming for magnetic field homogeneity. The MRI acquisition sequences were ordered as follows: one dMRI scan, two rsfMRI scans, and one T$_2$-weighted anatomical scan.

Diffusion weighted images were acquired using an 8-shot echo planar imaging (EPI) sequence with the following parameters: repetition time (TR) = 2500 ms; echo time (TE) = 25.88 ms; flip angle = 90°; max b-value = 900 s/mm^2; averages = 3; dummy scans = 2; directions = 42; slices = 12; coronal orientation; thickness = 0.75 mm; gap = 0 mm; field of view (FOV) = 19.2 × 19.2 mm; data acquisition matrix = 128 × 128 in-plane.

Resting-state fMRI was performed using a 2-shot EPI sequence with the following parameters: TR = 1000 ms; TE = 20 ms; repetitions = 210; flip angle = 90°; dummy scans = 4; slices = 12; coronal orientation; thickness = 0.75 mm; gap = 0 mm; FOV = 19.2 × 19.2 mm; data acquisition matrix = 64 × 64 in-plane.

Anatomical images were acquired using a fast-spin echo T$_2$-weighted imaging sequence with the following parameters: TR = 2000 ms; effective TE = 31.6 ms; echo spacing = 8.04; echo train length = 8 ms; slices = 12; coronal orientation; thickness = 0.75 mm; gap = 0 mm; FOV = 19.2 × 19.2 mm; data acquisition matrix = 192 × 192 in-plane.

2.3. Diffusion MRI pre-processing and statistical analysis

Diffusion MRI pre-processing and analysis was performed using previously described methods and a rodent-modified bi-tensor diffusion analysis pipeline (DeSimone et al., 2016; Pasternak et al., 2009). We used the FMRIB Software Library (FSL: Oxford, UK) and custom designed UNIX shell scripts in Analysis of Functional NeuroImages software (AFNI: Cox, 1996; Version 16.0.19, https://afni.nimh.nih.gov/afni/download/afni/psc_project_view) to correct for eddy current and head motion artifacts, compensation of diffusion gradient rotations in response to these corrections, and manual skull stripping for the removal of non-brain tissue. FW and FW-corrected diffusion tensor imaging (DTI) maps were calculated from the pre-processed motion and eddy current corrected volumes using custom code written in MATLAB (Version R2013a; The Mathworks, Natick, MA, USA). To create the FW map, a minimization procedure was used such that a bi-tensor model (Pasternak et al., 2009) was fit to each voxel in order to quantify FW fractional volume. The FW component is then eliminated from each

voxel to generate a FW-corrected mean diffusivity (MD_T) map. To standardize the data, the b0 image from each mouse was normalized to a single mouse b0 image using an affine transformation matrix and trilinear interpolation using the FSL Linear Image Registration Tool (FLIRT: http://fsl.fmrib.ox.ac.uk/fsl/fslwiki/FLIRT). The resultant transformation matrix was then applied to the FW, FA_T, and MD_T maps. Between-group comparisons were examined by submitting FW and MD_T values to voxel-wise independent-samples t-tests (i.e., cKO minus control) at an alpha level threshold of $P = 0.005$ using the 3dttest function in AFNI. We employed a Monte Carlo simulation using the 3dclustsim function in AFNI to estimate the required adjustment for multiple comparisons. Type I error adjustment was achieved by setting the significance level for the contrasts of interest to a voxel-level threshold of $P = 0.05$ corrected and minimum cluster size of 7 voxels.

2.4. Functional MRI pre-processing and statistical analysis

Functional MRI data pre-processing was performed using FSL and custom designed UNIX shell scripts in AFNI. To account for magnetization equilibrium, we discarded the initial 5 volumes of both EPI sequences and concatenated the remaining volumes into a single 410 volume sequence. All volumes were realigned to time point 0 of the acquisition. Data pre-processing additionally entailed manual skull stripping for the removal of non-brain tissue, and slice-timing and motion correction. To standardize the data, we co-registered the EPI image of each mouse brain to their respective T_2-weighted image, and then normalized the T_2-weighted image of each mouse to that of a single mouse brain. The resultant data matrix was applied to the EPI image via affine transformation with limited degrees of freedom and trilinear interpolation using FLIRT. Additionally, we performed spatial normalization and in-plane smoothing on the EPI image using a Gaussian FWHM kernel of 0.2 mm^2 (x-y planes) and filtered temporal data using a band-pass filter with a cut-off frequency between 0.01 and 0.1 Hz.

Functional MRI data were examined via seed-based FC analysis in AFNI using the general linear model approach and four bilateral seed regions of interest in the striatum (i.e., 8 total seed locations). Seed locations were selected a priori based on evidence of diminished FW and overlapping diffusivity changes in cKO mice (Fig. 1). Moreover, seed regions were consistent with established regions of cholinergic degeneration as a function of forebrain torsinA loss-of-function (Pappas et al., 2015). After obtaining the residual time series, we extracted the time series from the seed region and calculated Pearson's correlation coefficients across all brain voxels. The correlation coefficient was then transferred to a z-value, and the z-value extracted from each voxel provided a standardized measure of the degree of connectivity with each of the seeds from the striatum. Between-group comparisons were examined for each seed by submitting z-scores to voxel-wise independent-samples t-tests (i.e., cKO minus control) at an alpha level threshold of $P = 0.005$. A Monte Carlo simulation in AFNI yielded a significance level for the contrasts of interest to a voxel-level threshold of $P = 0.05$ corrected and a minimum cluster size of 31 voxels.

In a subsequent analysis, we sought to determine if FC values are robust in classifying mouse genotype (i.e., cKO, control). FC z-score values from a training cohort of 11 cKO and 11 control mice were submitted to a linear kernel support vector machine classification algorithm with 10-fold cross-validation using the Library for Support Vector Machines (LIBSVM: Chang and Lin, 2011). Classification reliability of the algorithm was evaluated in an independent testing cohort of 7 cKO and 7 control mice.

3. Results

3.1. Diffusion MRI: Free-water and mean diffusivity

A core feature of forebrain torsinA deletion in dystonic cKO mice is the marked degeneration and morphological adaptation of SCIs
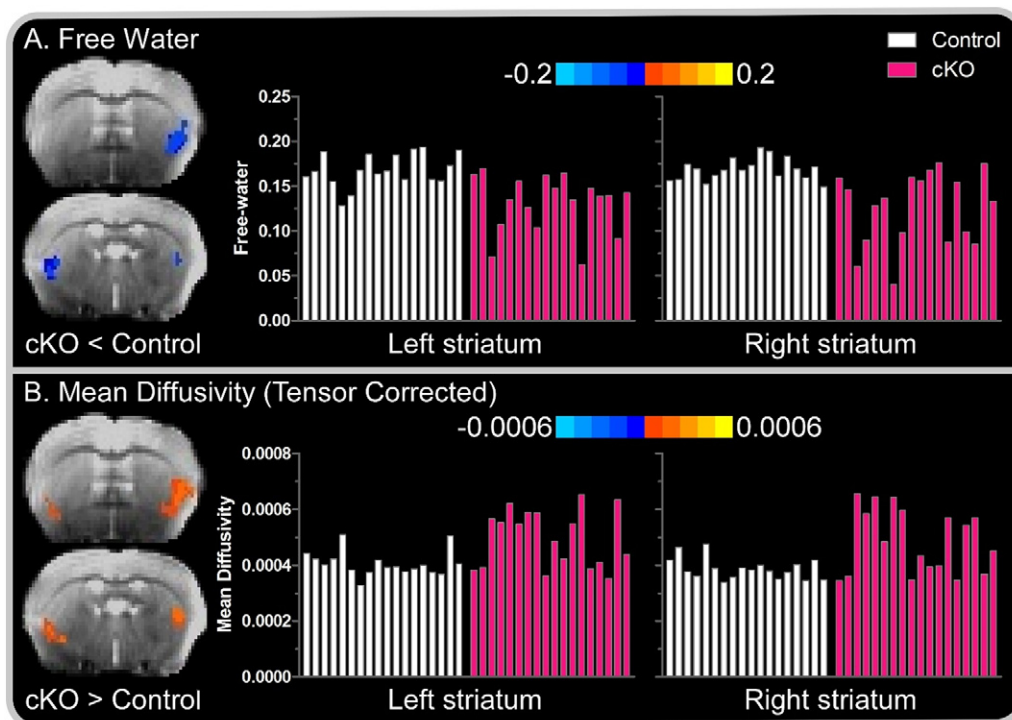

Fig. 1. Between-group striatal FW and MD_T. Color bars and maps represent the mean difference in FW and MD_T values for between-group post-hoc comparisons (i.e., cKO versus control). (A) Negative values, represented by cold (blue) colors superimposed over the b0 image of a single subject, denote a significant decrease in FW in cKO mice compared to controls in the left and right striatum. (B) Positive values, represented by warm (red) colors denote a significance increase in MD_T in cKO mice compared to controls in the left and right striatum. In each panel, subject-by-subject mean FW and MD_T values for the associated colored voxels are depicted by white and pink bars for control and cKO mice, respectively. Results are thresholded at $P < 0.005$ at the voxel-level and FWER corrected at $P < 0.05$.

(Pappas et al., 2015). We hypothesized that FW and MD_T may serve as a reflective marker of adaptations to tissue microstructure. To explore this possibility, we computed whole-brain FW and MD_T values and submitted values for cKO and control mice to voxel-wise independent samples t-tests. Consistent with our hypothesis, cKO mice demonstrated a significant decrease in FW relative to controls in the right and left striatum (all corrected $P < 0.05$). Conversely, MD_T was increased in the left and right striatum compared to that of controls (Fig. 1). FW and MD_T differences between cKO and control mice were confined to the striatum, consistent with prior studies demonstrating that the deletion of torsinA from forebrain cholinergic and GABAergic precursors imparts a striatum-specific structural lesion.

3.2. Correlation analysis: FW and MD_T

Compared to control mice, MD_T and FW values in dystonic cKO mice were increased and decreased, respectively. Notably, voxels expressing increased MD_T rendered a high degree of spatial overlap (i.e., 75%) with voxels wherein FW was reduced. To examine the relationship between tissue and extracellular derived diffusion indices, we computed Pearson's correlation coefficients between FW and MD_T values across common voxels in the striatum. Correlations between FW and MD_T values were examined separately for cKO and control groups. Analysis of MD_T values in cKO mice yielded significant, moderate-to-high inverse correlations with FW values in the left, right, and bilateral (i.e., averaged across right and left) striatum ($Ps < 0.005$) (Fig. 2). In contrast, correlation coefficients between MD_T and FW values in control mice failed to reach statistical significance.

3.3. Functional MRI: Increased whole-brain connectivity with striatum

Having localized aberrant tissue microstructure to the striatum, we sought to establish whether this abnormality influenced FC between the striatum and other brain regions. We first performed within-group t-tests independently for dystonic cKO and control mice for each of the eight striatal seed regions. In control mice, the striatum demonstrated a high degree of connectivity with brain regions ipsilateral to the seed location voxels, and significant negative correlation (i.e., anti-connectivity) with brain regions contralateral

to seed location voxels. Similarly, cKO mice demonstrated significantly increased FC between the striatal seed location and voxels within ipsilateral brain regions. However, unlike their control counterparts, the striatum in cKO mice demonstrated absent or significantly less extensive contralateral anti-connectivity than controls (Fig. 3). This pattern of seed-based connectivity of the striatum with ipsilateral and contralateral brain regions across cKO and control groups was observed for all seed locations.

We subsequently performed voxel-wise independent samples t-tests (i.e., cKO versus control) to examine group differences in FC independently for each of the eight striatal seed locations. FC differences between dystonic cKO and controls were more extensive for seeds originating in the left striatum compared to that of the right. For left seed locations, correlated clusters of functionally connected voxels extended across cortical, subcortical, cerebellar, and brainstem regions (all corrected $P < 0.05$). Compared to controls, cKO mice exhibited increased FC of the left striatum with multiple regions, including primary somatosensory cortex, thalamus, medial geniculate nucleus, superior colliculus, hippocampus, vermis, cerebellar nuclei (dentate and interposed), and anisiform and paramedian lobules (Figs. 4–5).

Between-group FC effects were less extensive for seeds originating in the right striatum as correlated clusters of functionally connected voxels were restricted to only cortical and subcortical regions. In particular, Fig. 6 shows that dystonic cKO mice demonstrated increased FC with the striatum in the thalamus, hypothalamus, midbrain (precommissural nucleus), primary somatosensory cortex, posterior parietal association area, and hippocampus.

We next performed a classification analysis based on the extracted z-scores from FC clusters revealed by between-group post-hoc analyses. Using a 10-fold cross validation support vector machine algorithm in randomly selected training and testing cohorts of 22 (11 cKO, 11 control) and 14 (7 cKO, 7 control) mice, respectively, single- and multi-cluster combinations yielded an area under the curve (AUC) between 0.73 and 0.91 in the training cohort, and moderate-to-high independent classification accuracy (71 to 100%) in the testing cohort. The results of the support vector machine analysis are presented in Table 1. This analysis indicates that the FC findings are robust in discriminating between mouse genotype.
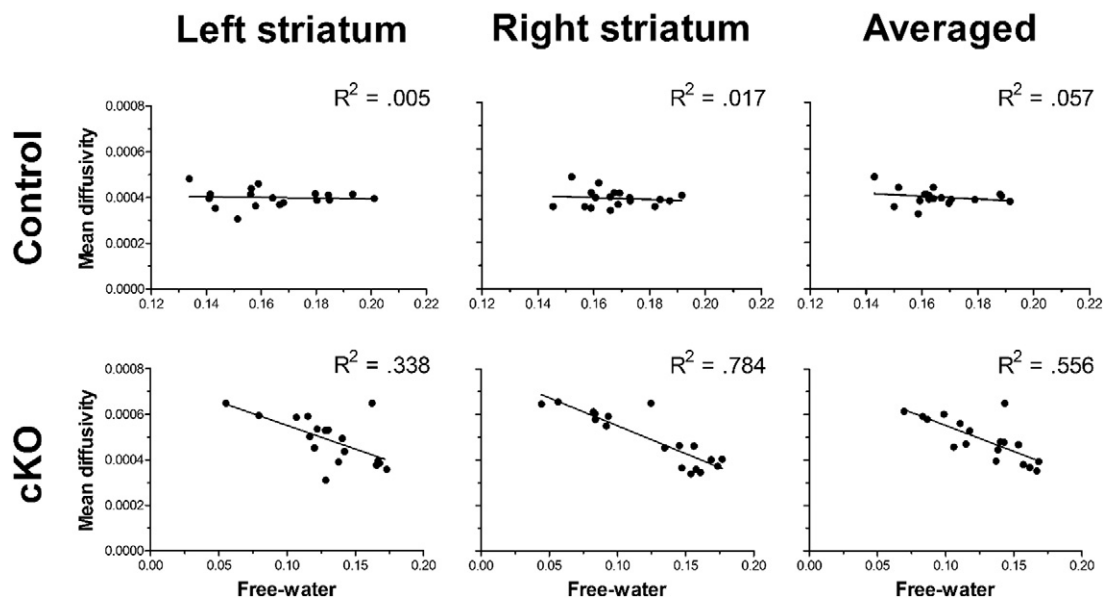

Fig. 2. FW and MD_T Pearson's correlation coefficients. Pearson correlations between mean FW values and MD_T in the striatum for control (top panel) and cKO (bottom panel) mice. Values for FW and MD_T were extracted from common voxels where between-group differences for each measure wereas detected. MD_T in the striatum yielded a significant moderate-to-high inverse correlation with FW values for cKO mice in the left and right striatum, as well as when averaged across both right and left striatum. FW and MD_T values in the striatum were not correlated in control mice.
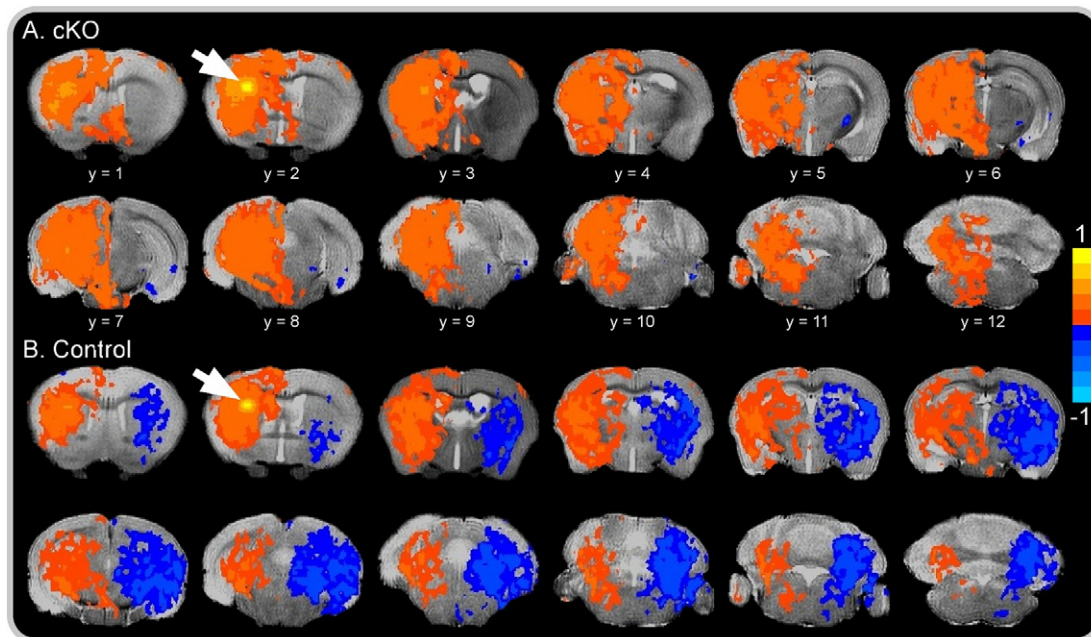
Fig. 3. Resting-state FC color maps. Spatial color coded z-maps for (A) cKO and (B) control mice of FC networks across all 12 brain slices originating from a single seed location (white arrow) in the left dorsolateral striatum. Positive values, represented by warm (red) colors, denote a significant increase in network-level functional connectivity with the seed location, whereas negative values, represented by cold (blue) colors, denote a significant decrease in FC with the seed location. Results are voxel-level thresholded at $P < 0.005$ and FWER corrected at $P < 0.05$. Color maps are superimposed over the T_2-weighted image of a single subject.

4. Discussion

Using multimodal imaging assays in an overtly symptomatic model of DYT1 dystonia that exhibits construct, face and therapeutic validity, we demonstrate a selective microstructural defect of the striatum and abnormal connectivity of this structure with cortical, subcortical, cerebellar, and brainstem regions. These observations establish a neuroimaging readout of direct and/or indirect neuronal adaptations to forebrain torsinA loss-of-function, and provide a set of connectivity abnormalities to be explored as pathophysiological substrates in DYT1 dystonia pathogenesis.

4.1. Reduced striatal FW in cKO mice

Our first objective was to determine whether abnormalities in extracellular and tissue derived diffusion indices may exist, reflecting striatal neurodegeneration or its consequences. Original work in the cKO mouse model found neurodegenerative effects of forebrain torsinA loss-of-function to be specific to SCIs, whereas the structural integrity of cortical and striatal GABAergic neurons was unaffected (Pappas et al., 2015). Given that post-mortem histological assays were not performed in cKO mice in the current study, it was important to employ a sensitive and alternative assay of microstructural adaptations to forebrain torsinA eradication. We utilized a bi-tensor diffusion pipeline to disentangle the diffusivity of brain tissue (MD_T) from that of extracellular FW (Pasternak et al., 2009, 2012). The bi-tensor technique provides a sensitive and reproducible measure of neurodegeneration and disease progression (Ofori et al., 2015; Pasternak et al., 2012; Planetta et al., 2016). This computational approach is important because it provides direct in vivo interpretation of neuropathological adaptations to torsinA loss and affords a direct translational metric that can be used to monitor such adaptations in human studies. Further, metrics derived from this analysis serve as a foundation for future in vivo studies examining longitudinal progression of pathology in animal models of DYT1 dystonia. Consistent with our hypothesis, striatal FW values in cKO mice were reduced relative to controls, suggesting extracellular volumetric decline in response to SCI hypertrophy. This finding is consistent with work using

a bi-tensor DTI model in acute concussion patients (Pasternak et al., 2014), which was interpreted to reflect regional trauma glial cell migration and swelling in injured areas. The reduced FW in the striatum of cKO mice is consistent with prior work demonstrating soma hypertrophy of surviving SCIs (Pappas et al., 2015) although it is possible that other mechanisms beyond SCI adaptation influence the FW metric.

In order to evaluate tissue specific water translation in the striatum, we quantified MD_T after correcting for FW contamination. MD_T provides an averaged multidirectional measure of diffusivity within grey matter and white matter tracts and is inversely related to cellular integrity (i.e., cellularity, swelling) (Alexander et al., 2011; Basser and Pierpaoli, 2011; Feldman et al., 2010; Pierpaoli et al., 1996). MD_T in cKO mice was increased in the left and right striatum of cKO mice relative to controls. This finding may reflect altered membrane depolarization resistance (i.e., increased cell capacitance) and cell soma hypertrophy in extant SCIs of cKO mice (Pappas et al., 2015). Indeed, cell capacitance (Fernández et al., 1982) is proportional to the insulator density of proteins that comprise the interstitial phospholipid bi-layer, and increased membrane density and inflammation can hinder directionally constrained cellular diffusion properties (Alexander et al., 2007, 2011).

FW and MD_T converged across a significant area of the striatum. Given that SCIs occupy a relatively small proportion of striatal cell types (Oorschot, 2013), assays derived from dMRI in the current study may reflect microstructural adaptations independent of SCI degeneration and altered morphology. In accounting for this discrepancy, we note that while forebrain regions exposed to torsinA eradication in cKO mice demonstrate no evidence of gliosis during initial development, it is possible that degenerative insult influenced post-developmental glial cell migration, thereby influencing partial volume effects (e.g., Pasternak et al., 2014; Wang et al., 2011). Alternatively, dendritic arborization, which is not incorporated into soma cell hypertrophy measures, may represent a compensatory mechanism following neurodegeneration in the striatum. Future progression studies aimed at combining in vivo imaging and post-mortem histological assays will prove important in furthering the current understanding on the relation between dMRI metrics and the effect of forebrain torsinA loss-of-function on microstructure of various cell types within the striatum.
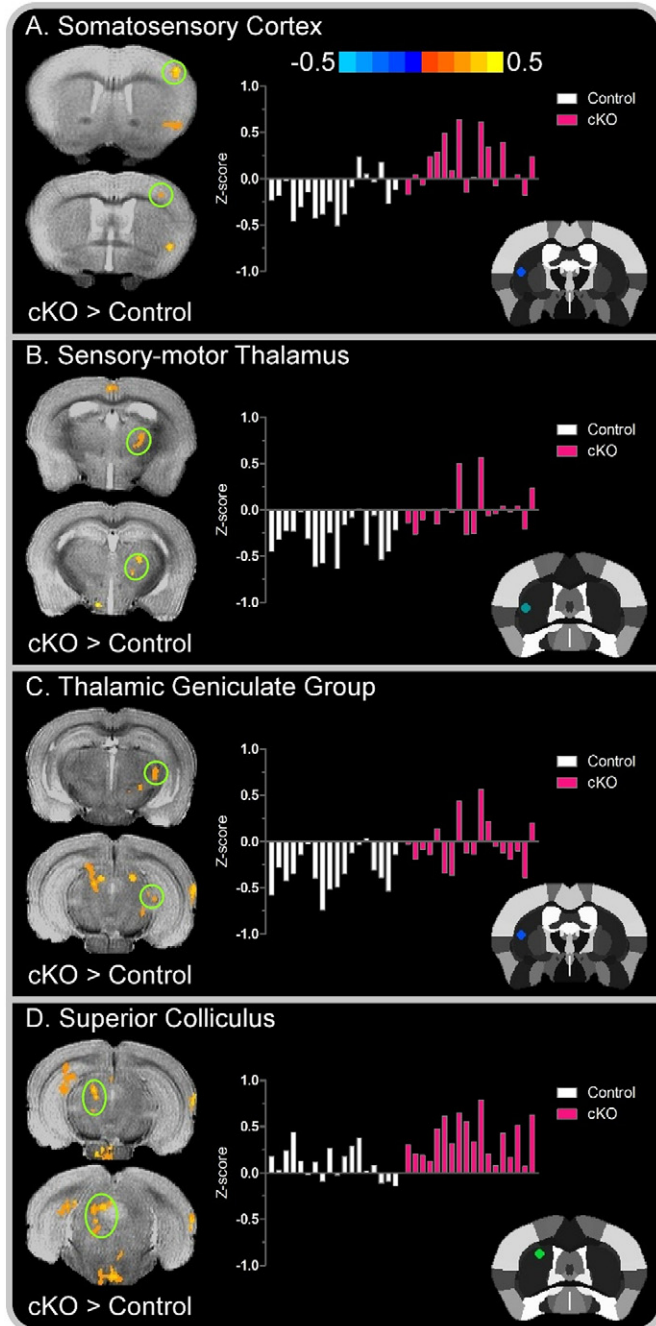
Fig. 4. Left seed cortical and subcortical between-group FC color maps. Color bar and spatial maps represent the mean difference in z-score values for cKO versus control mice. Cluster results are voxel-level thresholded at $P < 0.005$ and FWER corrected at $P < 0.05$. Positive values, represented by warm (red) colors denote a significant increase in FC for cKO mice in the (A) primary somatosensory cortex; (B) sensory-motor thalamus (C) thalamic geniculate group and (D) superior colliculus. FC clusters are superimposed over the T_2-weighted image of a single subject. The offset right bar plot in each panel depicts the subject-by-subject mean z-score values for the associated cluster in controls (white bars) and cKO mice (pink bars). The stereotaxic template atlas (Ferris et al., 2014) in each panel depicts the seed location within the left striatum wherein connectivity clusters originated.

Fig. 5. Left seed brainstem and cerebellar between-group FC color maps. Color bar and spatial maps represent the mean difference in z-score values for cKO versus control mice. Cluster results are voxel-level thresholded at $P < 0.005$ and FWER corrected at $P < 0.05$. Positive values, represented by warm (red) colors denote a significant increase in FC for cKO mice in the (A) Pons; (B) vermis; (C) cluster comprised of the vermis, cerebellar nuclei, and paramedian lobule; and (D) anisiform lobule. FC clusters are superimposed over the T_2-weighted image of a single subject. The offset right bar plot in each panel depicts the subject-by-subject mean z-score values for the associated cluster in controls (white bars) and cKO mice (pink bars). The stereotaxic template atlas (Ferris et al., 2014) in each panel depicts the seed location within the left striatum wherein connectivity clusters originated. Abbreviations included for the vermis, VERM; cerebellar nuclei, CN; and paramedian lobule, PaL.

4.2. Increased whole-brain connectivity with the striatum in cKO mice

The results provide direct in vivo support that dMRI can serve as a sensitive marker of striatal microstructural adaptation in response to forebrain torsinA loss. SCIs that do not degenerate in cKO mice have increased membrane capacitance, in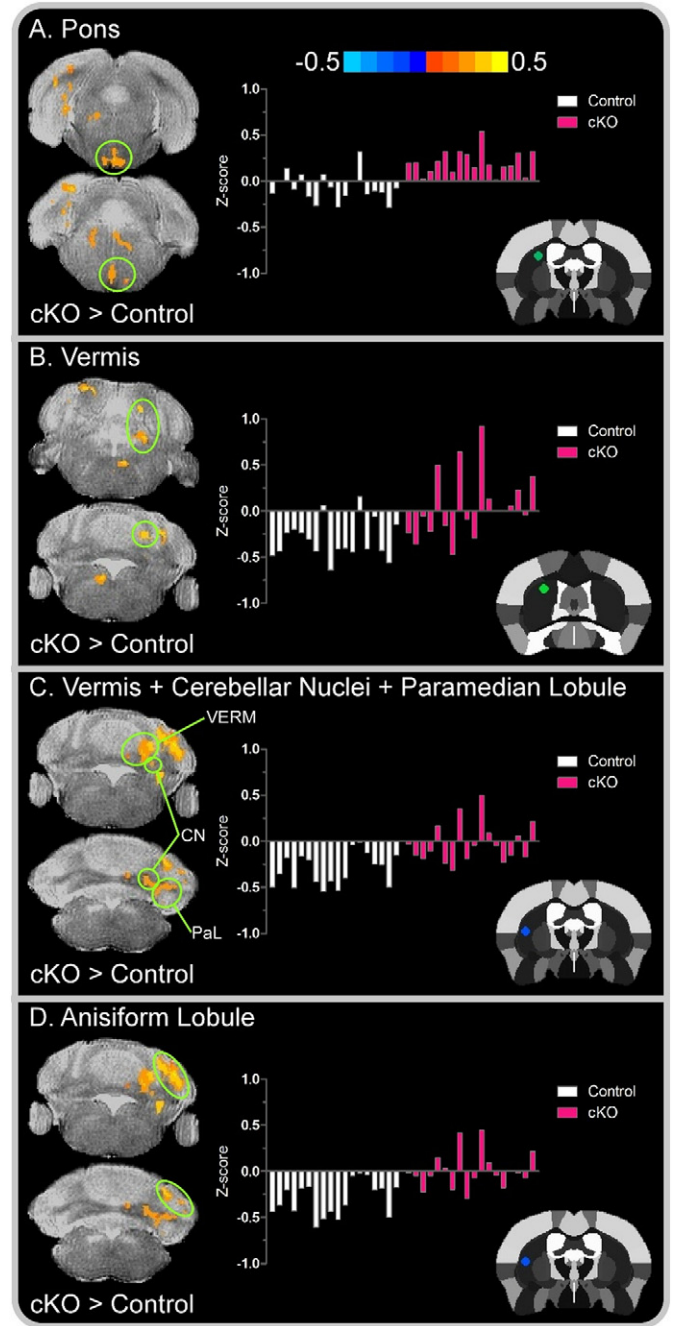creased spontaneous inhibitory post-synaptic currents, and hyperexcitation in response to depolarizing current pulses (Pappas et al., 2015). Consequently, we sought to determine whether striatal dysfunction triggers abnormalities in the temporal correlation between low-frequency fluctuations in resting-state blood oxygenation level dependent signal between the striatum and cortical,
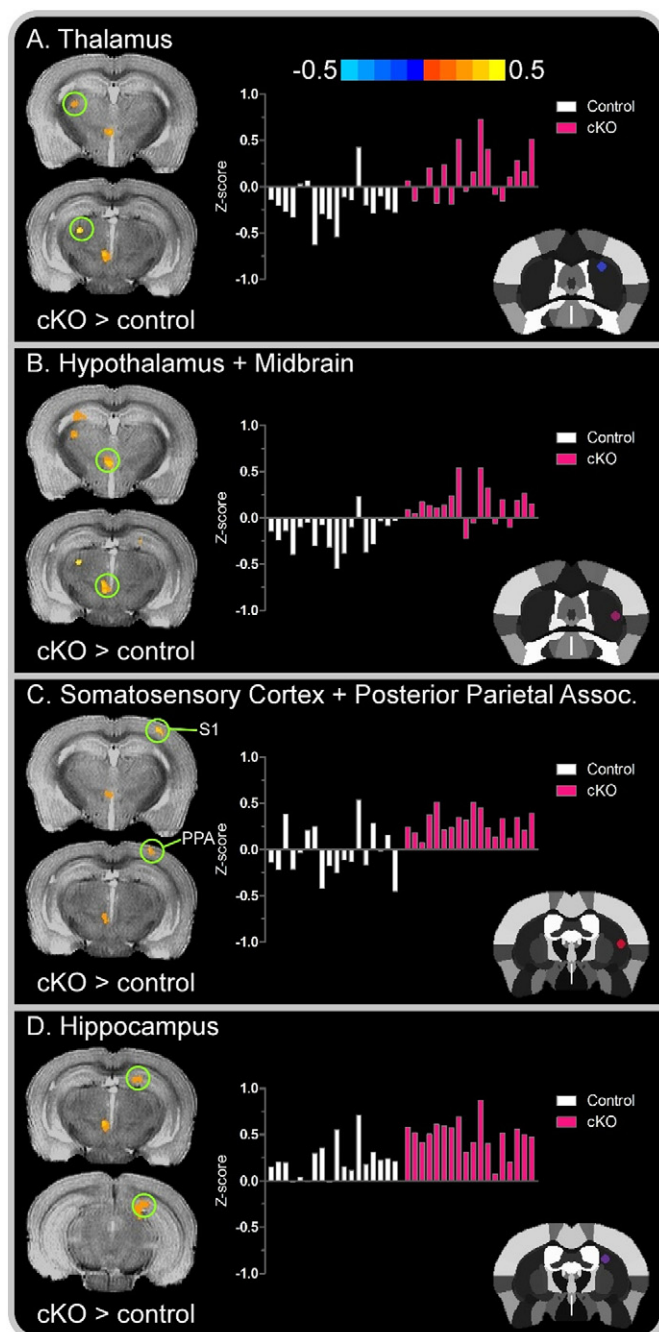
Fig. 6. Right seed cortical and subcortical between-group FC color maps. Color bar and spatial maps represent the mean difference in z-score values for cKO versus control mice. Cluster results are voxel-level thresholded at $P < 0.005$ and FWER corrected at $P < 0.05$. Positive values, represented by warm (red) colors denote a significant increase in FC for cKO mice in the (A) thalamus; (B) cluster comprised of the hypothalamus and midbrain; (C) cluster comprised of the primary somatosensory cortex and posterior parietal association area; and (D) hippocampus. FC clusters are superimposed over the T2-weighted image of a single subject. The offset right bar plot in each panel depicts the subject-by-subject mean z-score values for the associated cluster in controls (white bars) and cKO mice (pink bars). The stereotaxic template atlas (Ferris et al., 2014) in each panel depicts the seed location within the right striatum wherein connectivity clusters originated. Abbreviations included for the primary somatosensory cortex, S1; and posterior parietal association area, PPA.

subcortical, cerebellar, and brainstem regions. In addressing whole-brain network connectivity abnormalities in cKO mice we employed a region of interest approach to FC using four bilateral seeds (8 total) within the striatum.

Table 1

Summary of support vector machine classification model. Results are based on single- and multi-cluster FC mean z-score values in a training cohort of 11 cKO and 11 control mice, and evaluated in an independent testing cohort of 7 cKO and 7 control mice. AUC: receiver operating characteristic area under the curve representing sensitivity and specificity in the training cohort; Prediction: 10-fold cross validation classification accuracy in testing cohort. Common slashes separate adjacent regions that comprise a common single-cluster combination of voxels. Individual clusters within multi-cluster combinations are separated by addition signs (+).

Functional connectivity cluster(s)	AUC	Prediction
1. Somatosensory cortex	0.86	71.4
2. Sensory-motor thalamus	0.91	78.6
3. Superior colliculus	0.91	71.4
4. Pons	0.95	78.6
5. Vermis/cerebellar nuclei	0.91	71.4
6. Anisiform lobule	0.91	92.9
7. Thalamus	0.91	85.7
8. Somatosensory cortex + posterior parietal assoc.	0.83	64.3
9. Somatosensory cortex + sensory-motor thalamus	0.82	78.6
10. Somatosensory cortex + vermis/cerebellar nuclei	0.82	92.9
11. Somatosensory cortex + sensory-motor thalamus + vermis + vermis/cerebellar nuclei + anisiform lobule	0.75	92.9
12. Somatosensory cortex + thalamus + superior colliculus + anisiform lobule	0.75	100
13. Somatosensory cortex + sensory-motor thalamus + superior colliculus + anisiform lobule + vermis	0.73	100
14. Somatosensory cortex + hypothalamus/midbrain + geniculate group + anisiform lobule + vermis	0.74	100

Electrophysiological evidence of impaired bi-directional plasticity and synaptic integration within the cortico-striatal-thalamic pathway of overtly asymptomatic DYT1 mouse models has been related to a paradoxical increase in the activity of SCIs (Dang et al., 2012; Martella et al., 2009, 2014; Sciamanna et al., 2011, 2012a, 2012b; see also Eskow Jaunarajs et al., 2015). The current findings support cholinergic involvement in the compromised integrity of this major functional pathway in a symptomatic mouse model. In cKO mice studied here, forebrain eradication of torsinA from cholinergic and GABAergic neurons resulted in significantly increased striatal FC with the primary somatosensory cortex and thalamus. This is compatible with previous work using an exploratory-based independent component analysis (ICA) (DeSimone et al., 2016) showing increased FC in the striatum, thalamus, and somatosensory cortex in overtly asymptomatic DYT1 KI mice, which emulate the human DYT1 genotype (Dang et al., 2005). Additionally, this finding is consistent with positron emission tomography (PET) studies reporting sensorimotor hyperexcitability in symptomatically penetrant DYT1 patients compared to non-manifesting DYT1 carriers (Carbon et al., 2010). Moreover, studies using DTI and probabilistic tractography demonstrate that thalamocortical microstructural abnormalities appear to dichotomize symptomatic from asymptomatic DYT1 carriers (Argyelan et al., 2009; Vo et al., 2015b).

In addition to traditional models of basal ganglia dysfunction in DYT1 dystonia (Vitek, 2002; Vitek et al., 1999; Zhuang et al., 2004), a growing body of literature has implicated the cerebellum as a focal region of interest. Previous imaging studies in animal models of DYT1 dystonia have focused on the axonal tract of the cerebellothalmocortical pathway from a microstructural perspective; that is, imaging these tracts using DTI and probabilistic tractography ex vivo (e.g. Uluğ et al., 2011; Vo et al., 2015a). Tractography regions in these studies were selected on the basis of altered regional metabolic activity derived from changes in ex vivo FA and in vivo PET, and demonstrated reduced axonal fiber connectivity within cerebellothalamocortical and pontocerebellar tracts (Uluğ et al., 2011; Vo et al., 2015a). Similarly, we examined in vivo cerebellar and brainstem FC with the striatum based on striatal FW and diffusivity deficit, reflecting structural adaptations to forebrain torsinA loss-of-function. The striatum in cKO mice demonstrated increased FC with the cerebellar cortex (anisiform and paramedian lobules), vermis, cerebellar nuclei, and brainstem (pons, medulla).

These findings are consistent with prior studies in human and animal models of DYT1 dystonia. Increased striatal FC with a distant, yet connected cerebellum is in agreement with studies showing amelioration of cerebellar-induced dystonia when disynaptic interplay between the cerebellum and basal forebrain is interrupted (Chen et al., 2014; Neychev et al., 2008). The human DYT1 condition has been characterized by reduced FA in the dorsal pontine brainstem (Carbon et al., 2008b), which is thought to represent abnormalities of the cerebellothalamic tract, and increased cerebellar regional blood flow and metabolic activity (derived from in vivo PET) (Carbon et al., 2004; Carbon et al., 2008a; Carbon et al., 2010; Carbon and Eidelberg, 2009; Eidelberg et al., 1998). Based on DTI findings in human subjects, Eidelberg and colleagues (Argyelan et al., 2009; Niethammer et al., 2011; Vo et al., 2015b) suggested that disease penetrance depends on the presence of an abnormality of thalamocortical connectivity, with manifesting patients and non-manifesting mutation carriers respectively *lacking* or *exhibiting* a distal tract lesion. They interpreted these findings to suggest that a "second hit" prevents the cerebellothalamic defect from driving abnormal movements. A parallel set of studies in DYT1 KI and KO mice, which do not mimic dystonic features (and may represent the non-manifesting carrier condition), exhibited abnormalities of both cerebellothalamocortical and thalamocortical tracts (Uluğ et al., 2011; Vo et al., 2015a). Selective introduction of the heterozygous ΔE genotype in the hindbrain, however, did not produce the dystonic movements predicted by this model (Weisheit and Dauer, 2015). Studies in models of other forms of dystonia have also emphasized dysfunction of the cerebellar nuclei and Purkinje cells to be involved in generalized dystonia (Fremont et al., 2017; LeDoux et al., 1993, 1995, 1998; LeDoux and Lorden, 1998; Neychev et al., 2008). Moreover, altered FC was previously demonstrated in the anisiform and paramedian lobules of DYT1 KI mice using exploratory ICA in vivo (DeSimone et al., 2016).

The major finding from this study is that forebrain torsinA loss-of-function triggers whole-brain connectivity changes across cortical, subcortical, cerebellar, and brainstem functional networks in vivo. Unlike DYT1 KI mice, which exhibit subtle motor abnormalities (Dang et al., 2005), cKO mice spontaneously develop a dystonic-like twisting behavior responds to antimuscarinic therapies. Thus, forebrain eradication of torsinA in the cKO model affords developmental, behavioral, and therapeutic effects which are akin to the manifesting carrier state in human DYT1 dystonia (Pappas et al., 2015). The current study provides a foundation for future work examining therapeutic effects on FC in the cKO mouse model, which will prove important in understanding whether whole-brain FC reflects the disease-specific phenotypic correlation with the human condition or manifest as an endophenotype underlying forebrain torsinA dysfunction.

A final issue to address is whether striatal FC outcomes are explicitly dependent on altered structural and functional integrity of SCIs. Original work in the cKO mouse model found neurodegenerative, morphological, and functional effects of forebrain torsinA loss-of-function to be specific to SCIs, whereas the integrity and functionality of GABAergic neurons were unaffected (Pappas et al., 2015). It is possible, however, that regions in cKO mice unoccupied by cholinergic cell types (i.e., cortex) result in whole-brain FC changes. Such a finding would suggest that the suppression of GABAergic torsinA function could be partially responsible for whole-brain connectivity changes with regions containing both cholinergic and GABAergic cell types (i.e., striatum). Future studies evaluating multimodal imaging markers associated with the conditional knock-out of torsinA specific to GABAergic or cholinergic neurons will prove important in understanding the exact nature of FC outcomes derived from such cell types.

4.3. Conclusions

This study demonstrates increased striatal FC with cortical, subcortical, cerebellar, and brainstem functional circuits in a model of DYT1 dystonia exhibiting construct, face, and predictive validity. Increased FC across multiple cerebellar and brainstem regions in cKO mice in the absence of a cerebellar molecular lesion indicates the ability of forebrain-specific torsinA suppression to cause a whole-brain network-level FC impairment. Consistent with our previous work (DeSimone et al., 2016), we again find FW to be a sensitive measure of microstructural integrity in a mouse model of DYT1 dystonia.

Conflict of interest

The authors declare no competing financial interests.

References

Alexander, A.L., Lee, J.E., Lazar, M., Field, A.S., 2007. Diffusion tensor imaging of the brain. Neurotherapeutics 4, 316–329.
Alexander, A.L., Hurley, S.A., Samsonov, A.A., Adluru, N., Hosseinbor, A.P., Mossahebi, P., Tromp, D.P., Zakszewski, E., Field, A.S., 2011. Characterization of cerebral white matter properties using quantitative magnetic resonance imaging stains. Brain Connect. 1, 423–446.
Argyelan, M., Carbon, M., Niethammer, M., Uluğ, A.M., Voss, H.U., Bressman, S.B., Dhawan, V., Eidelberg, D., 2009. Cerebellothalamocortical connectivity regulates penetrance in dystonia. J. Neurosci. 29, 9740–9747.
Basser, P.J., Pierpaoli, C., 2011. Microstructural and physiological features of tissues elucidated by quantitative-diffusion-tensor MRI. J. Magn. Reson. 213, 560–570.
Battistella, G., Termsarasab, P., Ramdhani, R.A., Fuertinger, S., Simonyan, K., 2015. Isolated focal dystonia as a disorder of large-scale functional networks. Cereb. Cortex 27, 1203–1215.
Battistella, G., Fuertinger, S., Fleysher, L., Ozelius, L.J., Simonyan, K., 2016. Cortical sensorimotor alterations classify clinical phenotype and putative genotype of spasmodic dysphonia. Eur. J. Neurol. 23, 1517–1527.
Bhatia, K.P., Marsden, C.D., 1994. The behavioral and motor consequences of focal lesions of the basal ganglia in man. Brain 117, 859–876.
Biswal, B., Yetkin, F.Z., Haughton, V.M., Hyde, J.S., 1995. Functional connectivity in the motor cortex of resting human brain using echo-planar MRI. Magn. Reson. Med. 34, 537–541.
Breakefield, X.O., Blood, A.J., Li, Y., Hallett, M., Hanson, P.I., Standaert, D.G., 2008. The pathophysiological basis of dystonias. Nat. Rev. Neurosci. 9, 222–234.
Burton, K., Farrell, K., Li, D., Calne, D.B., 1984. Lesions of the putamen and dystonia: CT and magnetic resonance imaging. Neurology 34, 962–965.
Carbon, M., Eidelberg, D., 2009. Abnormal structure-function relationships in hereditary dystonia. Neuroscience 164, 220–229.
Carbon, M., Su, S., Dhawan, V., Raymond, D., Bressman, S., Eidelberg, D., 2004. Regional metabolism in primary torsion dystonia: effects of penetrance and genotype. Neurology 62, 1384–1390.
Carbon, M., Ghilardi, M.F., Argyelan, M., Dhawan, V., Bressman, S.B., Eidelberg, D., 2008a. Increased cerebellar activation during sequence learning in DYT1 carriers: an equiperformance study. Brain 131, 146–154.
Carbon, M., Kingsley, P.B., Tang, C., Bressman, S., Eidelberg, D., 2008b. Microstructural white matter changes in primary torsion dystonia. Mov. Disord. 23, 234–239.
Carbon, M., Argyelan, M., Habeck, C., Ghilardi, M.F., Fitzpatrick, T., Dhawan, V., Pourfar, M., Bressman, S.B., Eidelberg, D., 2010. Increased sensorimotor network activity in DYT1 dystonia: a functional imaging study. Brain 133, 690–700.
Chang, C.-C., Lin, C.-J., 2011. LIBSVM: a library for support vector machines. ACM Trans. Intell. Syst. Technol. 2, 27.
Chen, C.H., Fremont, R., Arteaga-Bracho, E.E., Khodakhah, K., 2014. Short latency cerebellar modulation of the basal ganglia. Nat. Neurosci. 17, 1767–1775.
Cox, R.W., 1996. AFNI: software for analysis and visualization of functional magnetic resonance neuroimages. Comput. Biomed. Res. 29, 162–173.
Dang, M.T., Yokoi, F., McNaught, K.S., Jengelley, T.A., Jackson, T., Li, J., Li, Y., 2005. Generation and characterization of Dyt1 DeltaGAG knock-in mouse as a model for early-onset dystonia. Exp. Neurol. 196, 452–463.
Dang, M.T., Yokoi, F., Cheetham, C.C., Lu, J., Vo, V., Lovinger, D.M., Li, Y., 2012. An anticholinergic reverses motor control and corticostriatal LTD deficits in Dyt1 ΔGAG knock-in mice. Behav. Brain Res. 226, 465–472.

DeSimone, J.C., Febo, M., Shukla, P., Ofori, E., Colon-Perez, L.M., Li, Y., Vaillancourt, D.E., 2016. In vivo imaging reveals impaired connectivity across cortical and subcortical networks in a mouse model of DYT1 dystonia. Neurobiol. Dis. 95, 35–45.

Eidelberg, D., Moeller, J.R., Antonini, A., Kazumata, K., Nakamura, T., Dhawan, V., Spetsieris, P., DeLeon, D., Bressman, S.B., Fahn, S., 1998. Functional brain networks in DYT1 dystonia. Ann. Neurol. 44, 303–312.

Eskow Jaunarajs, K.L., Bonsi, P., Chesselet, M.F., Standaert, D.G., Pisani, A., 2015. Striatal cholinergic dysfunction as a unifying theme in the pathophysiology of dystonia. Prog. Neurobiol. 127–128, 91–107.

Fahn, S., 1988. Concept and classification of dystonia. Adv. Neurol. 50, 1–8.

Fahn, S., Bressman, S.B., Marsden, C.D., 1998. Classification of dystonia. Adv. Neurol. 78, 1–10.

Feldman, H.M., Yeatman, J.D., Lee, E.S., Barde, L.H., Gaman-Bean, S., 2010. Diffusion tensor imaging: a review for pediatric researchers and clinicians. J. Dev. Behav. Pediatr. 31, 346–356.

Fernández, J.M., Bezanilla, F., Taylor, R.E., 1982. Distribution and kinetics of membrane depolarization. II. Frequency domain studies of gating currents. J. Gen. Physiol. 79, 41–67.

Ferris, C.F., Kulkarni, P., Toddes, S., Yee, J., Kenkel, W., Nedelman, M., 2014. Studies on the Q175 knock-in model of Huntington's disease using functional imaging in awake mice: evidence of olfactory dysfunction. Front. Neurol. 5, 94.

Ferron, J.-F., Kroeger, D., Chever, O., Amzica, F., 2009. Cortical inhibition during burst suppression induced with isoflurane anesthesia. J. Neurosci. 29, 9850–9860.

Fox, M.D., Snyder, A.Z., Vincent, J.L., Corbetta, M., Van Essen, D.C., Raichle, M.E., 2005. The human brain is intrinsically organized into dynamic, anticorrelated functional networks. Proc. Natl. Acad. Sci. U. S. A. 102, 9673–9678.

Fremont, R., Tewari, A., Angueyra, C., Khodakhah, K., 2017. A role for cerebellum in the hereditary dystonia DYT1. elife 6, e22775.

Fross, R.D., Martin, W., Li, D., Stoessl, A.J., Adam, M.J., Ruth, T.J., Pate, B.D., Burton, K., Calne, D.B., 1987. Lesions of the putamen: their relevance to dystonia. Neurology 37, 1125–1129.

Kupsch, A., Benecke, R., Müller, J., Trottenberg, T., Schneider, G.H., Poewe, W., Eisner, W., Wolters, A., Müller, J.U., Deuschl, G., Pinsker, M.O., Skogseid, I.M., Roeste, G.K., Vollmer-Haase, J., Brentrup, A., Krause, M., Tronnier, V., Schnitzler, A., Voges, J., Nikkhah, G., Vesper, J., Naumann, M., Volkmann, J., Deep-Brain Stimulation for Dystonia Study Group, 2006. Pallidal deep-brain stimulation in primary generalized or segmental dystonia. N. Engl. J. Med. 355, 1978–1990.

LeDoux, M.S., Lorden, J.F., 1998. Abnormal cerebellar output in the genetically dystonic rat. Adv. Neurol. 78, 63–78.

LeDoux, M.S., Lorden, J.F., Ervin, J.M., 1993. Cerebellectomy eliminates the motor syndrome of the genetically dystonic rat. Exp. Neurol. 120, 302–310.

LeDoux, M.S., Lorden, J.F., Meinzen-Derr, J., 1995. Selective elimination of cerebellar output in the genetically dystonic rat. Brain Res. 697, 91–103.

LeDoux, M.S., Hurst, D.C., Lorden, J.F., 1998. Single-unit activity of cerebellar nuclear cells in the awake genetically dystonic rat. Neuroscience 86, 533–545.

Liang, C.-C., Tanabe, L.M., Jou, S., Chi, F., Dauer, W.T., 2014. TorsinA hypofunction causes abnormal twisting movements and sensorimotor circuit neurodegeneration. J. Clin. Invest. 124, 3080–3092.

Liu, X., Zhu, X.-H., Zhang, Y., Chen, W., 2013. The change of functional connectivity specificity in rats under various anesthesia levels and its neural origin. Brain Topogr. 26, 363–377.

Maltese, M., Martella, G., Madeo, G., Fagiolo, I., Tassone, A., Ponterio, G., Sciamanna, G., Burbaud, P., Conn, P.J., Bonsi, P., Pisani, A., 2014. Anticholinergic drugs rescue synaptic plasticity in DYT1 dystonia: role of M_1 muscarinic receptors. Mov. Disord. 29, 1655–1665.

Marsden, C.D., Obeso, J.A., Zarranz, J.J., Lang, A.E., 1985. The anatomical basis of symptomatic hemidystonia. Brain 108, 463–483.

Martella, G., Tassone, A., Sciamanna, G., Platania, P., Cuomo, D., Viscomi, M.T., Bonsi, P., Cacci, E., Biagioni, S., Usiello, A., Bernardi, G., Sharma, N., Standaert, D.G., Pisani, A., 2009. Impairment of bidirectional synaptic plasticity in the striatum of a mouse model of DYT1 dystonia: role of endogenous acetylcholine. Brain 132, 2336–2349.

Martella, G., Maltese, M., Nistico, R., Schirinzi, T., Madeo, G., Sciamanna, G., Ponterio, G., Cacci, E., Biagioni, S., Usiello, A., Bernardi, G., Sharma, N., Standaert, D.G., Pisani, A., 2014. Regional specificity of synaptic plasticity in a knock-in mouse model of DYT1 dystonia. Neurobiol. Dis. 65, 124–132.

Metzler-Baddeley, C., O'Sullivan, M.J., Bells, S., Pasternak, O., Jones, D.K., 2012. How and how not to correct for CSF-contamination in diffusion MRI. NeuroImage 59, 1394–1403.

Neychev, V.K., Fan, X., Mitev, V.I., Hess, E.J., Jinnah, H.A., 2008. The basal ganglia and cerebellum interact in the expression of dystonic movement. Brain 131, 2499–2509.

Niethammer, M., Carbon, M., Argyelan, M., Eidelberg, D., 2011. Hereditary dystonia as a neurodevelopmental circuit disorder: evidence from neuroimaging. Neurobiol. Dis. 42, 202–209.

Ofori, E., Pasternak, O., Planetta, P.J., Li, H., Burciu, R.G., Snyder, A.F., Lai, S., Okun, M.S., Vaillancourt, D.E., 2015. Longitudinal changes in free-water within the substantia nigra of Parkinson's disease. Brain 138, 2322–2331.

Oorschot, D.E., 2013. The percentage of interneurons in the dorsal striatum of the rat, cat, monkey, and human: a critique of the evidence. Basal Ganglia 3, 19–24.

Ostrem, J.L., Markun, L.C., Glass, G.A., Racine, C.A., Volz, M.M., Heath, S.L., de Hemptinne, C., Starr, P.A., 2014. Effect of frequency on subthalamic nucleus deep brain stimulation in primary dystonia. Parkinsonism Relat. Disord. 20, 432–438.

Ozelius, L., Lubarr, N., 1993. In: Pagon, R.A., Adam, M.P., Ardinger, H.H., Wallace, S.E., Amemiya, A., Bean, L.J.H., Bird, T.D., Ledbetter, N., Mefford, H.C., Smith, R.J.H., Stephens, K. (Eds.), DYT1 Early-onset Isolated Dystonia. GeneReviews, Seattle (WA). University of Washington, Seattle.

Ozelius, L.J., Hewett, J.W., Page, C.E., Bressman, S.B., Kramer, P.L., Shalish, C., De Leon, D., Brin, M.F., Raymond, D., Corey, D.P., 1997. The early-onset torsion dystonia gene (DYT1) encodes an ATP-binding protein. Nat. Genet. 17, 40–48.

Pappas, S.S., Darr, K., Holley, S.M., Cepeda, C., Mabrouk, O.S., Wong, J.M., LeWitt, T.M., Paudel, R., Houlden, H., Kennedy, R.T., Levine, M.S., Dauer, W.T., 2015. Forebrain deletion of the dystonia protein torsinA causes dystonic-like movements and loss of striatal cholinergic neurons. elife 4, e08352.

Pasternak, O., Sochen, N., Gur, Y., Intrator, N., Assaf, Y., 2009. Free water elimination and mapping from diffusion MRI. Magn. Reson. Med. 62, 717–730.

Pasternak, O., Westin, C.F., Bouix, S., Seidman, L.J., Goldstein, J.M., Woo, T.U., Petryshen, T.L., Mesholam-Gately, R.I., McCarley, R.W., Kikinis, R., Shenton, M.E., Kubicki, M., 2012. Excessive extracellular volume reveals a neurodegenerative pattern in schizophrenia onset. J. Neurosci. 32, 17365–17372.

Pasternak, O., Koerte, I.K., Bouix, S., Fredman, E., Sasaki, T., Mayinger, M., Helmer, K.G., Johnson, A.M., Holmes, J.D., Forwell, L.A., 2014. Hockey concussion education project, part 2. Microstructural white matter alterations in acutely concussed ice hockey players: a longitudinal free-water MRI study. J. Neurosurg. 120, 873–881.

Pierpaoli, C., Jezzard, P., Basser, P.J., Barnett, A., Di Chiro, G., 1996. Diffusion tensor MR imaging of the human brain. Radiology 201, 637–648.

Pisani, A., Martella, G., Tscherter, A., Bonsi, P., Sharma, N., Bernardi, G., Standaert, D.G., 2006. Altered responses to dopaminergic D2 receptor activation and N-type calcium currents in striatal cholinergic interneurons in a mouse model of DYT1 dystonia. Neurobiol. Dis. 24, 318–325.

Planetta, P.J., Ofori, E., Pasternak, O., Burciu, R.G., Shukla, P., DeSimone, J.C., Okun, M.S., McFarland, N.R., Vaillancourt, D.E., 2016. Free-water imaging in Parkinson's disease and atypical parkinsonism. Brain 139, 495–508.

Sciamanna, G., Tassone, A., Martella, G., Mandolesi, G., Puglisi, F., Cuomo, D., Madeo, G., Ponterio, G., Standaert, D.G., Bonsi, P., 2011. Developmental profile of the aberrant dopamine D2 receptor response in striatal cholinergic interneurons in DYT1 dystonia. PLoS One 6, e24261.

Sciamanna, G., Hollis, R., Ball, C., Martella, G., Tassone, A., Marshall, A., Parsons, D., Li, X., Yokoi, F., Zhang, L., 2012a. Cholinergic dysregulation produced by selective inactivation of the dystonia-associated protein torsinA. Neurobiol. Dis. 47, 416–427.

Sciamanna, G., Tassone, A., Mandolesi, G., Puglisi, F., Ponterio, G., Martella, G., Madeo, G., Bernardi, G., Standaert, D.G., Bonsi, P., 2012b. Cholinergic dysfunction alters synaptic integration between thalamostriatal and corticostriatal inputs in DYT1 dystonia. J. Neurosci. 32, 11991–12004.

Uluğ, A.M., Vo, A., Argyelan, M., Tanabe, L., Schiffer, W.K., Dewey, S., Dauer, W.T., Eidelberg, D., 2011. Cerebellothalamocortical pathway abnormalities in torsinA DYT1 knock-in mice. Proc. Natl. Acad. Sci. U. S. A. 108, 6638–6643.

Vidailhet, M., Vercueil, L., Houeto, J.L., Krystkowiak, P., Benabid, A.L., Cornu, P., Lagrange, C., Tézenas du Montcel, S., Dormont, D., Grand, S., Blond, S., Detante, O., Pillon, B., Ardouin, C., Agid, Y., Destée, A., Pollak, P., French Stimulation du Pallidum Interne dans la Dystonie (SPIDY) Study Group, 2005. Bilateral deep-brain stimulation of the globus pallidus in primary generalized dystonia. N. Engl. J. Med. 352, 459–467.

Vitek, J.L., 2002. Pathophysiology of dystonia: a neuronal model. Mov. Disord. 17 (Suppl. 3), S49–S62.

Vitek, J.L., Chockkan, V., Zhang, J.Y., Kaneoke, Y., Evatt, M., DeLong, M.R., Triche, S., Mewes, K., Hashimoto, T., Bakay, R.A., 1999. Neuronal activity in the basal ganglia in patients with generalized dystonia and hemiballismus. Ann. Neurol. 46, 22–35.

Vo, A., Sako, W., Dewey, S.L., Eidelberg, D., Uluğ, A.M., 2015a. 18FDG-microPET and MR DTI findings in Tor1a +/− heterozygous knock-out mice. Neurobiol. Dis. 73, 399–406.

Vo, A., Sako, W., Niethammer, M., Carbon, M., Bressman, S.B., Uluğ, A.M., Eidelberg, D., 2015b. Thalamocortical connectivity correlates with phenotypic variability in dystonia. Cereb. Cortex 25, 3086–3094.

Wang, Y., Wang, Q., Haldar, J.P., Yeh, F.C., Xie, M., Sun, P., Tu, T.W., Trinkaus, K., Klein, R.S., Cross, A.H., Song, S.K., 2011. Quantification of increased cellularity during inflammatory demyelination. Brain 134, 3590–3601.

Weisheit, C.E., Dauer, W.T., 2015. A novel conditional knock-in approach defines molecular and circuit effects of the DYT1 dystonia mutation. Hum. Mol. Genet. 24, 6459–6472.

Zhuang, P., Li, Y., Hallett, M., 2004. Neuronal activity in the basal ganglia and thalamus in patients with dystonia. Clin. Neurophysiol. 115, 2542–2557.